Article

Secondary Phase CeO$_2$ Precipitates in Ce,Er-Doped Na$_{0.5}$La$_{0.5}$MoO$_4$ Single Crystals Grown by Czochralski Method

Elena I. Suvorova [1,*] **, Kirill A. Subbotin** [2,3] **, Denis A. Lis** [2] **, Evgeny V. Zharikov** [2] **and Philippe A. Buffat** [4]

[1] A.V. Shubnikov Institute of Crystallography, Federal Scientific Research Centre "Crystallography and Photonics" of the Russian Academy of Sciences, Leninsky 59, Moscow 119333, Russia

[2] Prokhorov General Physics Institute, Russian Academy of Sciences, Moscow 119991, Russia; soubbot@lsk.gpi.ru (K.A.S.); lisdenis@mail.ru (D.A.L.); evzh@mail.ru (E.V.Z.)

[3] Faculty of Technology of Inorganic Substances and High-Temperature Materials, Mendeleev University of Chemical Technology, Moscow 125047, Russia

[4] Ecole Polytechnique Fédérale de Lausanne, Centre Interdisciplinaire de Microscopie Electronique, CH-1015 Lausanne, Switzerland; philippe.buffat@epfl.ch

* Correspondence: suvorova@crys.ras.ru

Abstract: Analytical scanning and transmission electron microscopy were used to study the microstructure of Ce,Er-doped Na$_{0.5}$La$_{0.5}$MoO$_4$ laser crystals. Crystals were grown by the Czochralski method from the melts with a nominal composition of Na$_{0.5}$La$_{0.5-x}$Ce$_x$Er$_{0.005}$MoO$_4$, where x = 0.125 and 0.15, then annealed at 700 and 1000 °C in the oxidizing atmosphere. We found the secondary phase precipitation of Ce$_2$O$_3$ oxide in as-grown crystals, while after high-temperature annealing the CeO$_2$ precipitated crystals are always observed. Impurity ions Ce^{3+} occupy the La sites, and approximately 20% of the nominal Ce content is involved in the formation of Ce oxide secondary phase precipitates. The length of CeO$_2$ precipitated crystals ranged between 100 nm and 550 nm (average length was 200 nm) and their width was 30–70 nm. The mechanism of CeO$_2$ formation is discussed. The orientation relationships of Na$_{0.5}$La$_{0.5-x}$Ce$_x$Er$_{0.005}$MoO$_4$/CeO$_2$, the degree of coherence of the interface, and the preferential directions of their growth in the matrix were established. CeO$_2$ crystals precipitated in the matrix cause light scattering with a wavelength comparable to the size of the precipitates and lead to deterioration of optical transparency of the material.

Keywords: Ce-Er-doped Na$_{0.5}$La$_{0.5}$MoO$_4$ (NLM); Ce$_2$O$_3$ and CeO$_2$ secondary phase precipitates; annealing; transmission electron microscopy; electron diffraction; energy dispersive X-ray spectrometry; electron energy loss spectroscopy

1. Introduction

Materials having clear transparency without noticeable absorption or scattering are often important for use in extreme mechanical and/or thermal conditions. Second phase precipitation, inclusion trapping, pores, point defects, color centers, and other imperfections in single crystals are still a serious problem today [1,2]. The use of such crystals in optics, laser technology, scintillators, and other applications may be very limited or even prevented due to the scattering of light caused by these defects. The solution to this problem is linked to the study of the causes and mechanisms of the formation of these defects and lies in optimizing the crystal production process. Na$_{0.5}$La$_{0.5}$MoO$_4$ (NLM) is a representative of big family of double molybdates and tungstates, with the general formula NaX^{3+}(MoO$_4$)$_2$ (X = Ln^{3+} and Y^{3+}), which are well-known host materials for laser and phosphor ions which belong to a scheelite type disordered structure with tetragonal symmetry [3]. This disordered structure has more advantages, like higher concentration rare-earth ion doping than ordered structures, a strong charge transfer band near the UV region, and good thermal and chemical stability [4–6]. It was believed that doped laser crystals could be grown at practically any concentration of the active dopants due to the similarity of the ionic radius

and, consequently, the complete substitution of Re ions in the crystal lattice [3,7,8]. In our work, using the example of Ce^{3+},Er^{3+}-doped $Na_{0.5}La_{0.5}MoO_4$ (NLM), we show that the concentrations of impurities of trivalent rare earth ions cannot be arbitrarily large, and that some parts of the doping ions tend to agglomerate and form precipitates along dislocations in the matrix structure. Post-growth annealing, performed for thermal stress relaxation in grown matrix crystals, leads to secondary phase precipitation. We believe that it is important to identify this, since heterogeneity induced by inclusions/precipitates causes absorption and scattering, which degrades system performance. The choice of a $Na_{0.5}La_{0.5}MoO_4$ single crystal is due to its considerable interest as a gain medium for diode-pumped solid-state lasers [8], while Ce^{3+} and Er^{3+} co-doping leads to a significant increase in the 1.5-μm luminescence efficiency [9,10].

As a rule, the powder X-ray diffraction method was widely used to study the phase composition of laser materials, and the use of scanning electron microscopy was supposed to confirm their structural homogeneity. Obviously, such a characterization is incomplete, so it seems quite surprising that transmission electron microscopy methods are not used to study the microstructure of laser materials. The present study of the real structure of the Ce^{3+},Er^{3+}-doped NLM at the nanoscale and the observation of defects as a possible reason of crystal opacity have confirmed the strong need to use methods of analytical scanning and transmission electron microscopy (SEM, TEM), including electron diffraction, energy-dispersive X-ray spectrometry (EDXS), and electron energy loss spectroscopy (EELS) for the characterization of the morphology, sizes, and orientation of possible precipitates, interphase interfaces, and their coherency with the matrix.

2. Materials and Methods

The crystals were grown by the Czochralski method from the melts of the nominal compositions $Na_{0.5}La_{0.5-x}Ce_xEr_{0.005}MoO_4$ (x = 0.125 and 0.150; the x values correspond to 2.1 and 2.5 at.% Ce) in an inductively heated iridium crucible in 98 vol% N_2 + 2 vol% O_2 atmosphere on the [001] NLM oriented seeds, with a pulling rate 3.0 ± 0.5 mm/h. Extra-pure grade sodium carbonate and metal oxide precursors were used. The as-grown crystals were annealed in air at 700 and 1000 °C for 72 h and then cooled to room temperature. More information about the crystal growth is available elsewhere [11,12].

The powder X-ray diffraction (XRD) patterns were obtained using a DRON-3M and DRON 6 diffractometers (IC Burevestnik, S-Petersburg, Russia) with Cu*Kα* radiation in the range of 2θ = 15°–100° and a scan step of 0.02°. Phase analysis using the Rietveld method was performed in the PDWin program (Technosoft Bilgisayar Yazilim, Istanbul, Turkey).

Overview images in the secondary and backscattered electron imaging modes were recorded together with the EDXS (energy dispersive X-ray spectrometry) chemical microanalysis of the matrix crystal in an FEI XL30 SFEG electron high-resolution scanning microscope (FEI, Hillsboro, OR, USA) fitted with an Oxford Instruments SDD INCA EDXS using a 15–20 kV accelerating voltage.

Specimens for TEM were cut from non-annealed and annealed samples, and mechanically polished and thinned by conventional Ar ion milling (Gatan PIPS, Pleasanton, CA, USA) at room temperature. TEM and STEM (scanning TEM) images, EDXS microanalysis, electron energy lost spectroscopy (EELS) data, and selected area electron diffraction (SAED) patterns were obtained at 300 kV accelerating voltage on an analytical field emission transmission electron microscope CM300 UT-FEG (FEI, Hillsboro, OR, USA). To estimate the thickness of the TEM samples, we first estimated the Mo/O concentration ratio in the matrix on the raw material by EDXS, then introduced an absorption correction into the EDXS analysis of the TEM foil with a thickness such that it led to the same Mo/O ratio. The standardless element microanalysis carried out on bulky samples in SEM showed a stable stoichiometric ratio Mo:O $\cong$ 1:4 in MoO_4^{2-}, when ZAF (Z = Atomic number effect, A = Self-absorption effect, F = Fluorescence effect) correction [13] was applied to quantify the elements. The Cliff-Lorimer ratio method [14] used for element quantification in TEM was matching the MoO_4^{2-} stoichiometry adjusting the thickness of the samples to this

ratio. Finally, the estimated thickness was in a reasonable range from 50 to 100 nm and satisfactorily corresponded to the stoichiometric composition within the statistical error bar.

TEM (HRTEM) images and SAED patterns were processed with the DigitalMicrograph suite GMS 2.31 (Gatan Inc, Pleasanton, CA, USA). Crystal phase identification, HRTEM image simulation, and diffraction analysis were performed with the JEMS software [15]. Simulation of powder X-ray diffraction patterns of Ce oxides and NLM mixtures with different ratios (without introducing background) was conducted using the CaRIne Crystallography v.3.1 of Cyrille Boudias and Daniel Monceau software [16].

3. Results

The SEM and TEM EDXS results showed that, on average, the Ce concentration in the as-grown matrix is always lower than the nominal concentration in the melt by about 0.20 ± 0.05 at.%. It does not change after annealing within the statistical measurement error. This means that the segregation coefficient (the ratio of the concentration of an impurity in a liquid to the concentration of an impurity in a solid) is slightly less than 1. This may also indicate the formation of secondary phases.

Therefore, the phase composition of the samples, both as-grown and annealed, was first studied by X-ray diffraction (XRD). Analysis of the experimental X-ray diffraction patterns using the Rietveld refinement did not show the presence of any secondary phases (see for instance [11]). It could be assumed that the formed cerium oxide precipitates were not detected on the XRD patterns due to the complete overlap of the peaks from the precipitates and the matrix, as well as peak broadening due to the presence of the strains and stresses in the samples. Therefore, XRD patterns were simulated using experimental concentrations of Ce oxide (Figure 1) and the known lattice parameters of tetragonal $I4_1a$ NLM [8], cubic Fm-3m CeO_2 [17], and trigonal P-3m1 Ce_2O_3 [18].
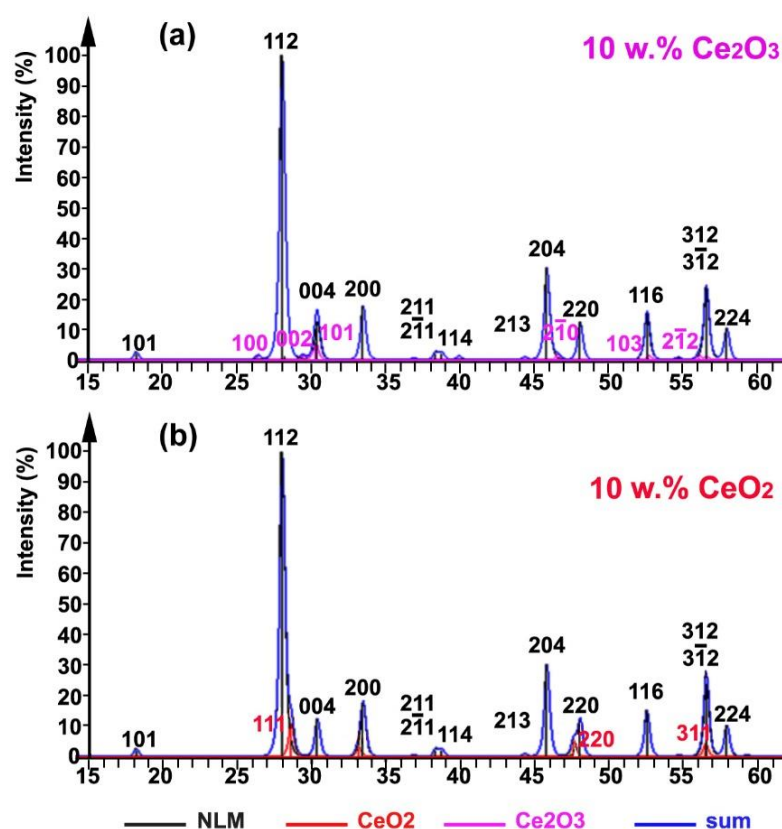

Figure 1. Simulated XRD patterns from the mixture of NLM:Ce_2O_3 = 90 w.%:10 w.% before annealing (**a**) from the mixture of NLM:CeO_2 = 92 w.%:10 w.% after annealing (**b**). NLM and sum are barely distinguished at 27°.

Simulation (Figure 1) of the XRD patterns of NLM + Ce_2O_3 and NLM + CeO_2 mixtures (Ce concentrations were taken close to the experimental ones) showed completely overlapping diffraction maximums with a small change in peak shape. Therefore, the Ce oxide secondary phases are below the XRD detection limit despite the observed deterioration of optical transparency [11].

Figure 2 shows the 15 kV BSE SEM images of the surface of the fractured $Na_{0.5}La_{0.370}Ce_{0.125}Er_{0.005}MoO_4$ crystal before (Figure 2a) and after annealing (Figure 2b) containing precipitates. Precipitates in the as-grown NLM are up to 200×20 nm with a low contrast shown in Figure 2a. In the annealed matrix, in addition, new precipitates appeared with larger sizes ranging from 100 nm to 550 nm and a higher contrast that tells they extend deeper (Figure 2b).
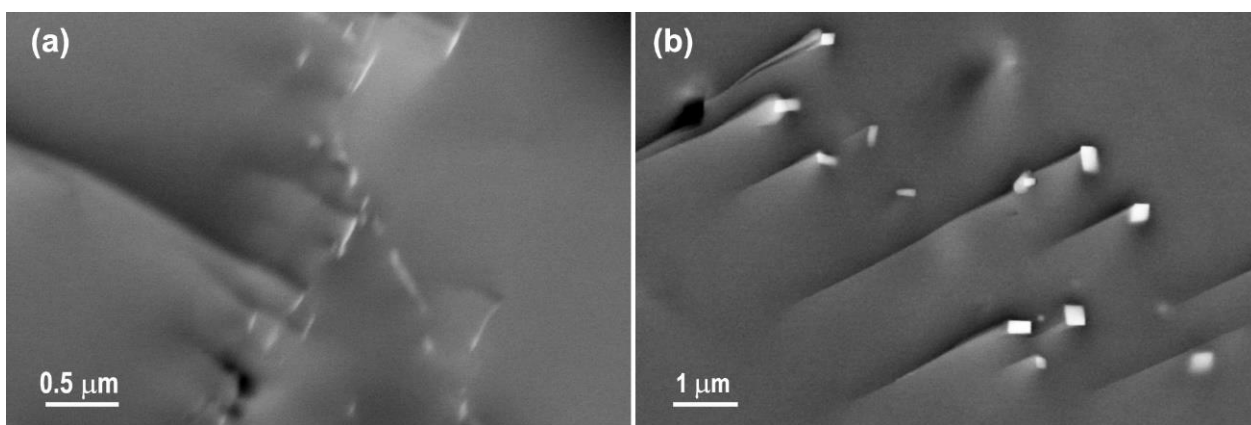

Figure 2. SEM BSE images of cleaved $Na_{0.5}La_{0.037}Ce_{0.125}Er_{0.005}MoO_4$ crystals before (**a**) and after (**b**) annealing.

The CeO_2 precipitates are distributed over the matrix crystal very heterogeneously and often formed chains. Their density distribution is about 1–5 crystals/μm^3 as estimated from several tens of SEM images recorded at an accelerating voltage of 10–15 kV which corresponds to a $\approx 1\ \mu m$ depth of investigation. Additionally, the density increases with an increase in the nominal Ce concentration.

Transmission electron microscopy aims to bring answers to the valence status of Ce in the matrix before and after annealing, the concentration of Ce in the matrix, the phase composition of precipitates, and the amount of cerium impurity is involved in the formation of precipitates.

Figure 3 shows a bright field TEM image of a dislocation in the non-annealed NLM matrix. EDXS showed that the average concentrations in area 1 (matrix) and 2 (defect) are, respectively, 1.8 at.% and 2.2 at.%.

Careful analysis of the reflection intensities on the SAED pattern (Figure 3b) shows that they cannot be understood, regardless of sample thickness and tilt, if only the NLM lattice is taken into account. Considering that Ce impurities may have segregated to this dislocation position to form a Ce_2O_3 crystal, a lattice overlap may occur. Taking in account the very close interplanar spacings for the pairs of planes $d_{(004)\ NLM} = 0.2934$ nm and $d_{(-110-1)\ Ce2O3} = 0.2945$ nm, as well for $d_{(3-12)\ NLM} = 0.1624$ nm and $d_{(20-21)\ Ce2O3} = 0.1623$ nm we conclude that the reflections $[130](00\bar{4})$NLM match $[\bar{1}5\bar{4}6](\bar{1}10\bar{1})$ Ce_2O_3, and the crystal is tilted about $2.38°$ in the direction of $(\bar{3}1\ 14)$ NLM plane with a Laue center circle CLC at $(-4.903, 1.634, 21.98)$. The lattice misfit is so small that there is no visible deformation in the image. EELS spectra (Figure 3c) obtained from matrix and defect areas confirmed that Ce has a valence 3+ and was not oxidized during crystal growth.
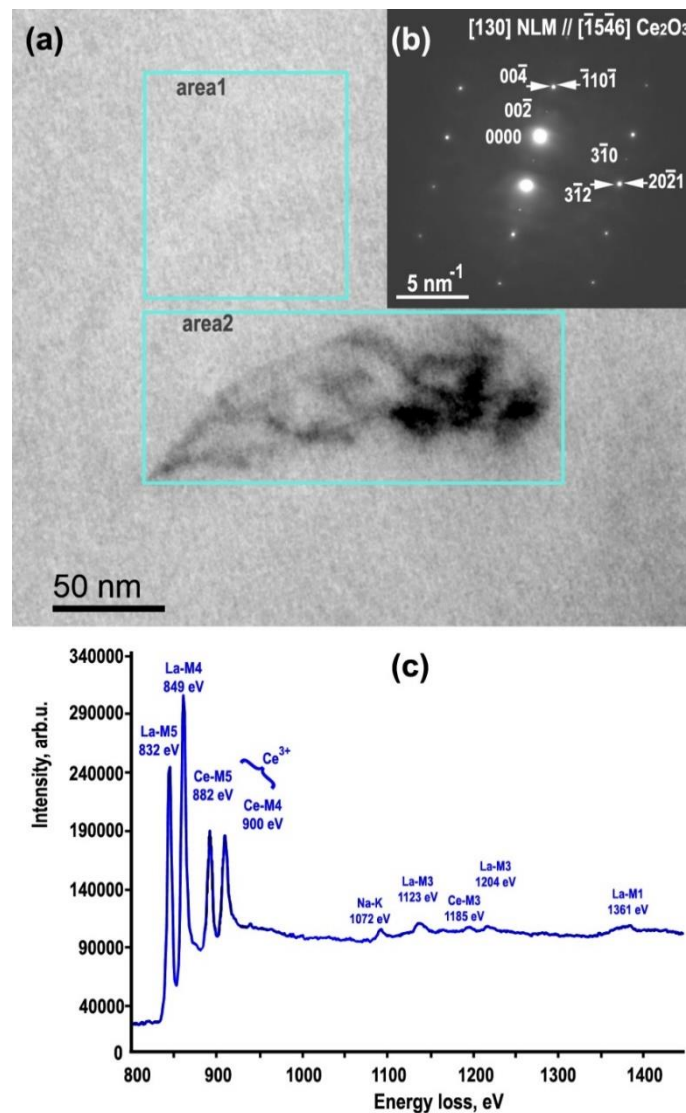
Figure 3. (**a**) Non−annealed sample: TEM image with two marked rectangle areas (blue) where chemical composition was obtained: area 1 is a matrix and area 2 contains dislocations, (**b**) SAED pattern obtained from the full image, (**c**) EELS spectrum with all edges of present elements obtained in the areas 1 and 2.

The EELS spectra of Ce^{4+} and Ce^{3+} are different [19]. Figure 4a shows a TEM image with precipitates. Only Ce^{3+} was found in our NLM lattice, while only Ce^{4+} is seen in the precipitates after annealing (the blue arrows indicate on Figure 4b,c the places where EELS spectra were obtained). The onset of Ce^{3+}-$M_{5,4}$ edges are at 882.0 and 899.7 eV (Figure 4b) while Ce^{4+}-$M_{5,4}$ edges (Figure 4c) are shifted to higher energy and characterized by two strong maxima at 884.0 and 901.6 eV. Additionally, two broad, weak maxima are present at 889.2 and 906.7 eV in Ce^{4+} EELS spectrum. In addition, the intensity of M_5 Ce^{3+} edge is higher than that of M_5 edge of Ce^{4+}.

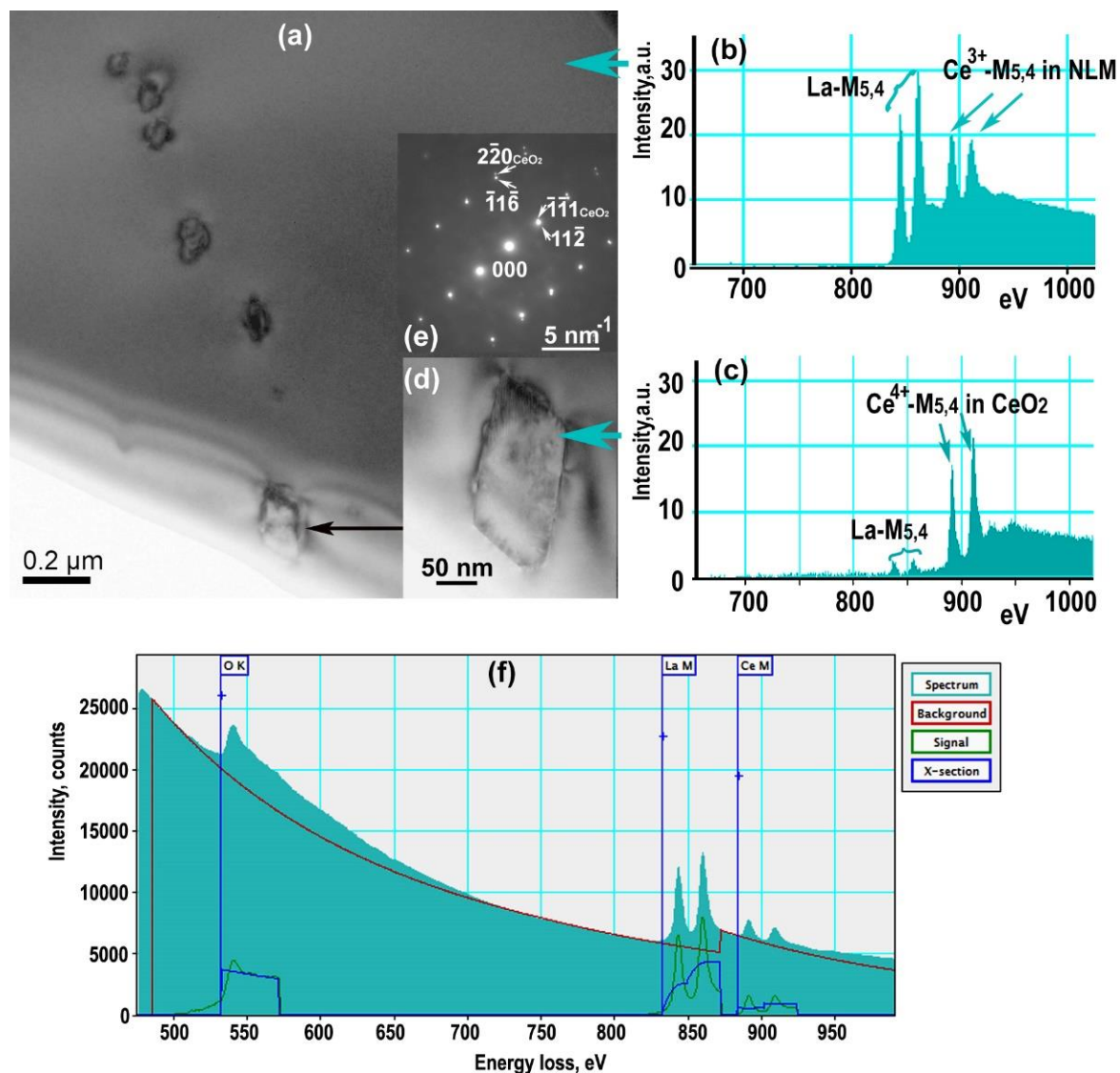**Figure 4.** (**a**)TEM image with precipitated crystals after annealing, (**b**) EELS spectra obtained from the matrix with Ce^{3+}, and from the precipitate with Ce^{4+}, (**c**) CeO_2 crystal, (**d**) and the corresponding SAED pattern with reflections from NLM and CeO_2 obtained along $[\bar{2}41]$NLM$//[112]CeO_2$ directions, (**e**) EELS spectrum obtained from the matrix, and (**f**) used to quantify the amount of Ce.

The SAED pattern obtained from the precipitated crystal (Figure 4d,e) confirmed the CeO_2 phase. The Ce concentration relative to La (Ce/La) in the doped NLM matrix was determined from EELS spectra (Figure 4f) using polynomial or power low background model. The average experimental ratio Ce/La (from 20 EELS spectra) was found to be 0.28 ± 0.05 for the $Na_{0.5}La_{0.370}Ce_{0.125}Er_{0.005}MoO_4$ matrix. Assuming that the nominal ratio between cerium a nd lanthanum remained at the level of $0.125/0.37 \approx 0.34$, then the rough estimate of the amount of cerium used for the formation of precipitates is about 20% of the total amount of the introduced Ce impurity.

Precipitation may easily occur both heterogeneously at the dislocations and, apparently, homogeneously within the matrix [20]. Figure 5 shows the bright and dark field TEM images of precipitated crystals which occurred along dislocations and in the NLM matrix.

It was described in [21] that the morphology of the growing particle/crystal is determined by the lattice misfit between precipitates and matrix.
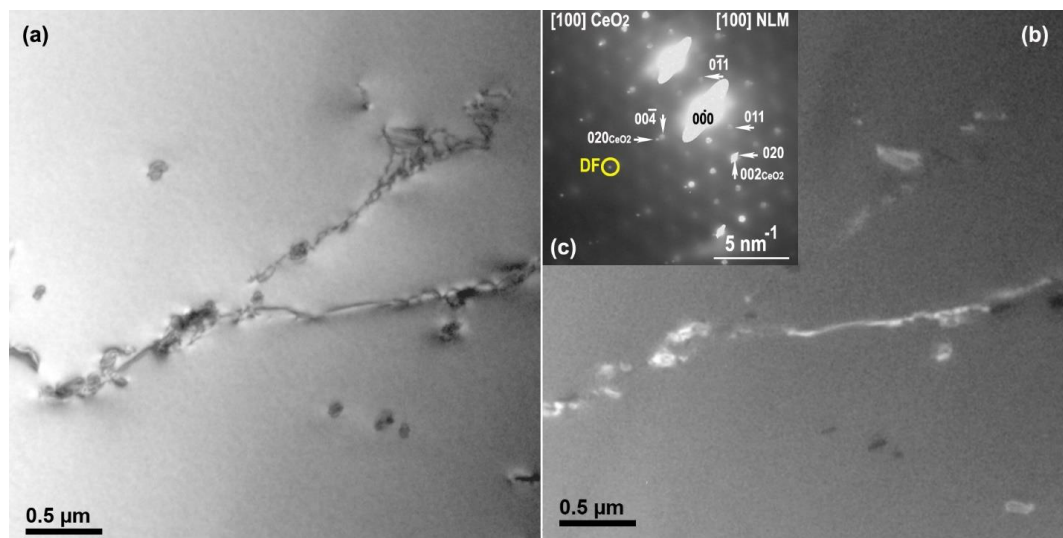
Figure 5. TEM bright field (**a**) and dark field (**b**) images showing the precipitation along dislocations and precipitation in the matrix (the CeO_2 crystal the right bottom corner), the corresponding SAED pattern (**c**) from NLM and CeO_2, the 040 CeO_2 reflection (in the circle) was used to obtain the DF TEM.

The typical shape of the CeO_2 crystals is shown in Figure 6a, the length of the crystal is 186 nm and the width is 50 nm. The following orientation relationships can be derived from the SAED pattern (Figure 6b):
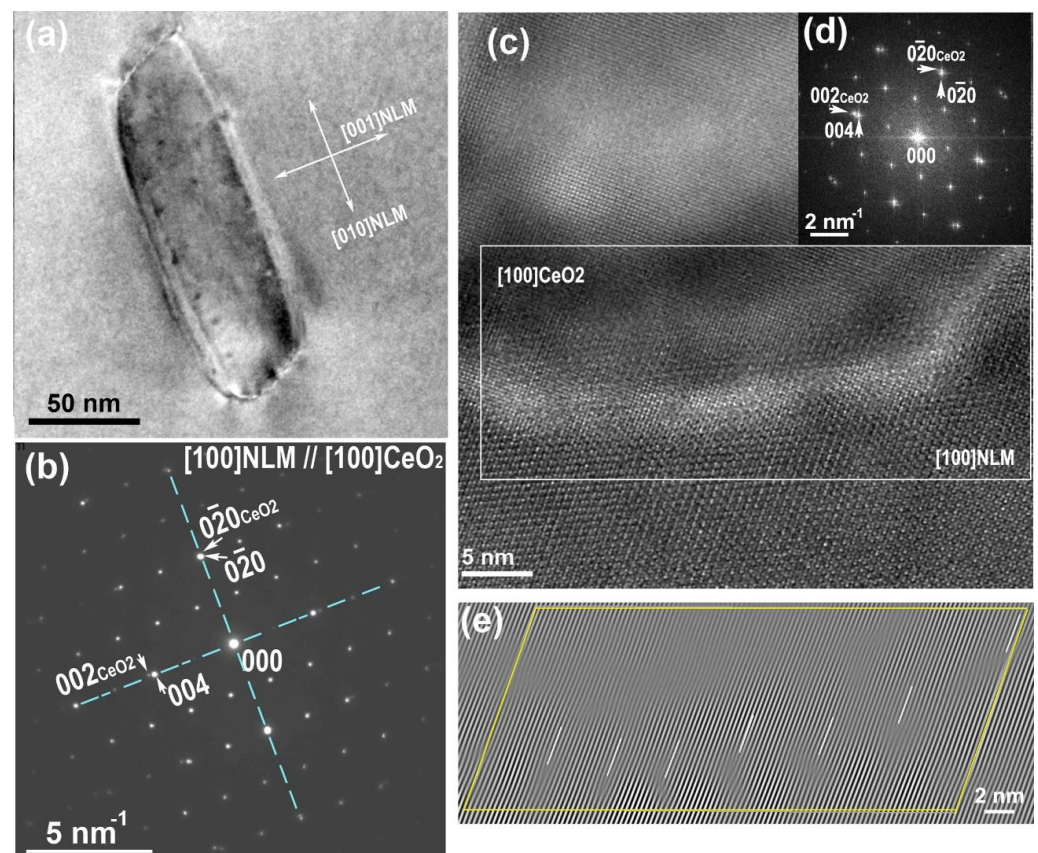

Figure 6. TEM image of CeO_2 crystal (**a**) and the corresponding SAED pattern (**b**), HRTEM image of the CeO_2/NLM demi−coherent interface (**c**), HRTEM FFT (**d**) and inverse FFT (IFFT) image with misfit dislocations (**e**) obtained selecting the 002 CeO_2 reflections.

[100](001)NLM//<100>{001}CeO$_2$
[010](001)NLM//<100>{001}CeO$_2$.

The CeO$_2$/NLM interface is demi-coherent with misfit dislocations (Figure 6e). At the interface, seven (002) CeO$_2$ extra planes are inserted over 100 (004) NLM planes. The lattice misfit between 002 CeO$_2$ and 004 NLM planes is about 7.0%, while the misfit between 020 CeO$_2$ and 020 NLM is about 0.9%. (Figure 6e).

The precipitated CeO$_2$ crystals grow to a size at which coherency is no longer maintained, and the critical length at which coherency is lost is about 180–200 nm. Figure 7 shows a CeO$_2$ crystal with a length of 550 nm. We can see from the SAED pattern (Figure 7b) that (020) and (002) CeO$_2$ planes are not parallel to the (020) and (004) NLM planes, correspondingly. An angle of 1.6° appeared between the planes, as indicated on the SAED diagram. The EDXS element maps confirm the presence of O, Na, Mo, La, and Ce and the quantification leads to the composition of CeO$_2$ crystal.
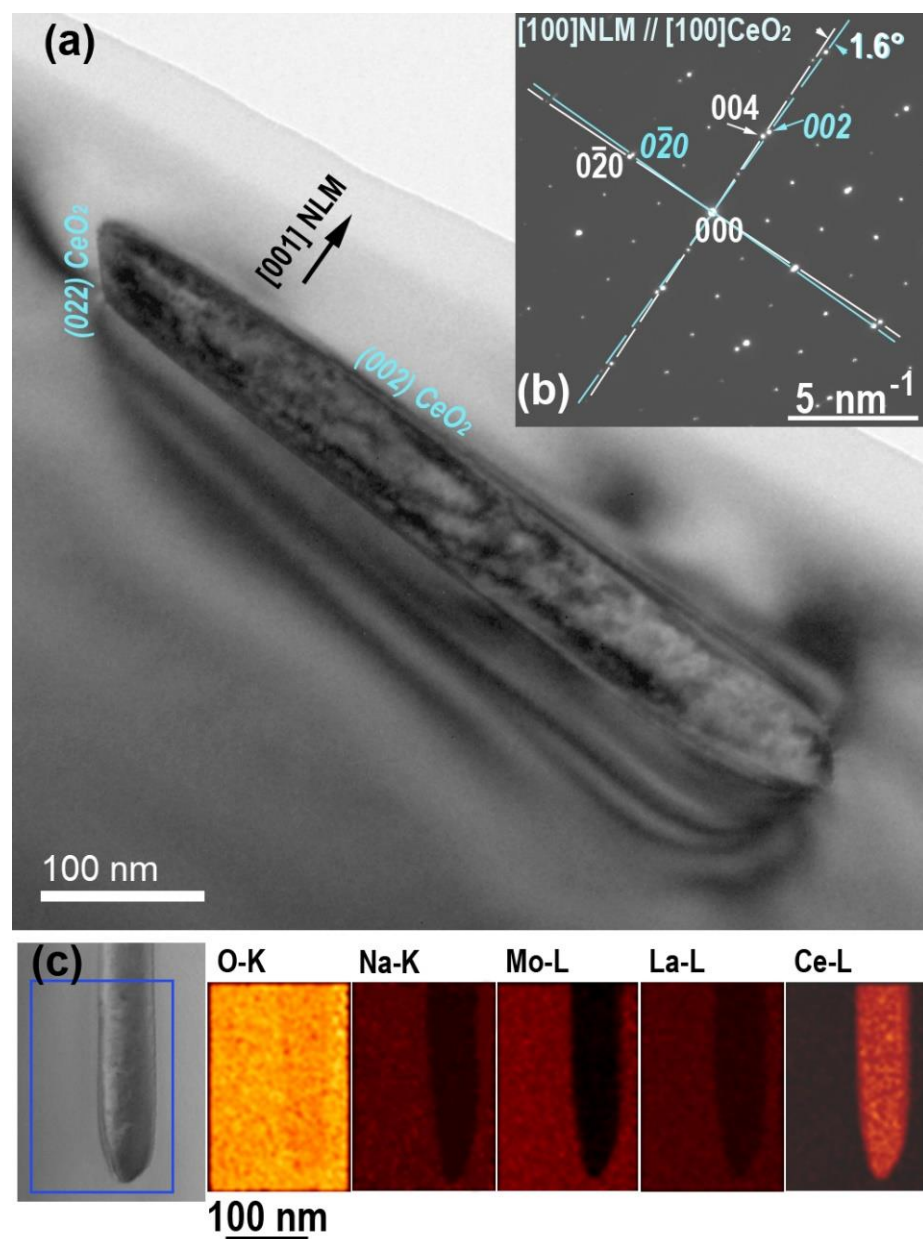

Figure 7. TEM image of a CeO$_2$ crystal 550 nm long (**a**) the corresponding SAED pattern (**b**) showing the twist between matrix and precipitates planes to relax misfit and STEM image (**c**) with the corresponding EDXS element maps of O, Na, Mo, La and Ce.

Figures [6] and [7] show that CeO_2 precipitates grow predominantly in the [100] and [010] NLM directions. In addition, another set of preferred growth directions for precipitates was observed, namely along [0 ± 51] NLM, i.e., by adding $(0\bar{1}1)$ or (011) NLM planes, as shown in Figure [8]. Perfect agreement would require a rotation of 1.8° between the two gratings. This is only compensated by strain in the smallest precipitates (Figure [6]) and becomes apparent in the largest (Figure [7]). These precipitates are also slightly misoriented relative to the main direction in NLM; however, the rotation angle is about 0.5°.
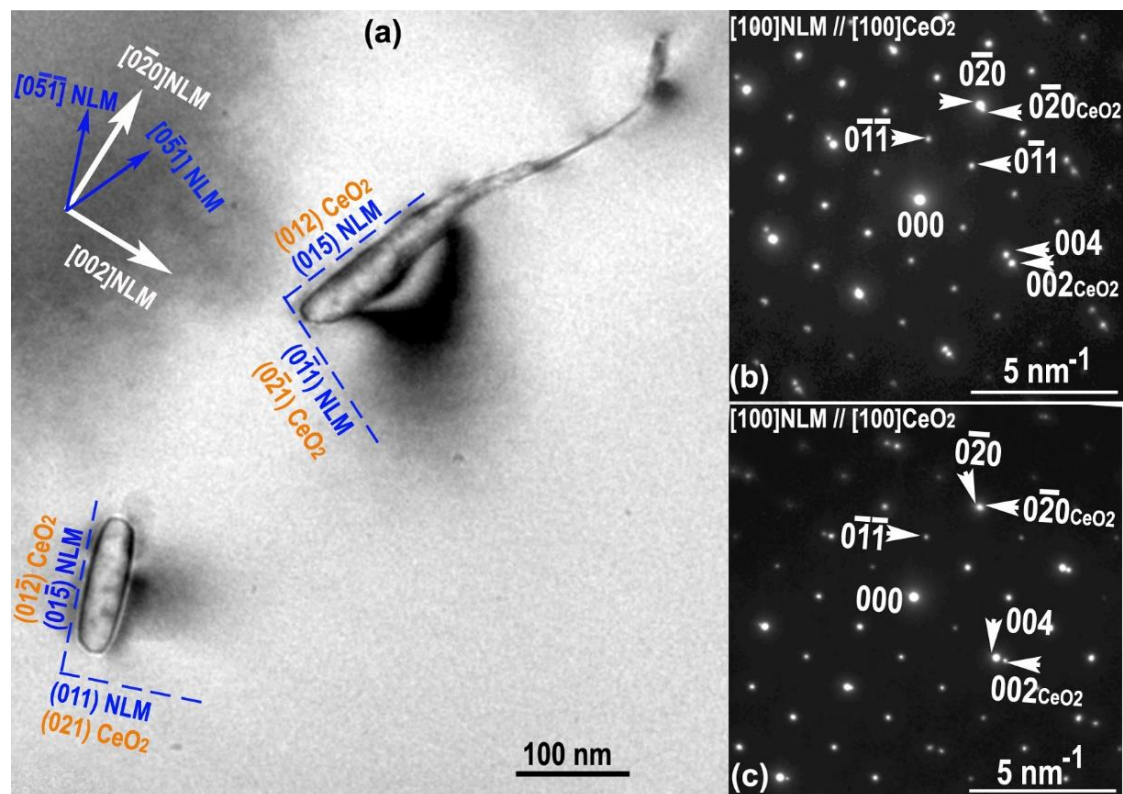

Figure 8. TEM image of two CeO_2 crystals showing the preferred [051] and $[0\bar{5}1]$NLM growth directions in the matrix with the (015) and $(01\bar{5})$ NLM interface planes (**a**) and the corresponding SAED patterns obtained along [100]NLM//[100]CeO_2 (**b,c**).

4. Discussion and Conclusions

TEM images suggest that the nucleation of precipitates in NLM can be mainly heterogeneous on dislocations. In as-grown NLM matrices, EDXS measurements reveal some Ce-rich areas along the dislocations, which EELS confirmed to be Ce^{3+}. In accordance with the SAED patterns, the Ce_2O_3 phase was identified and lattice misfit between two phases is very small.

The phase transformation from precipitated $Ce^{3+}_2O_3$ to $Ce^{4+}O_2$ occurred during 72 h of high (700 °C and 1000 °C) temperature annealing. The Ce^{3+} ions in the NLM lattice were not oxidized.

The length of most precipitated CeO_2 crystals ranged between 100 nm and 550 nm (average length is 200 nm) and their width was 30–70 nm.

It was estimated that about 20% of the nominal Ce content in the melt is involved in the formation of Ce_2O_3 precipitates, which transform into CeO_2 after annealing. The small CeO_2 precipitates up to 180 nm in length have nearly perfect orientation relationships with the NLM matrix at the interface between (020) and (200) NLM and {020}CeO_2 planes with the misfit of about 0.9% which means the presence of one misfit dislocations over 100 planes. Meanwhile, the misfit between (004) NLM and (002) CeO_2 planes reached 8.5% which requires one CeO_2 extra plane approximately over 12 NLM planes.

The preferential growth directions of CeO_2 crystal growth are parallel to NLM [100], [010], or [0 ± 51] NLM. The CeO_2 crystals of about 180 nm in length and longer are losing the coherency with the NLM matrix and the corresponding planes are no longer parallel to each other. The angle of rotation reaches $1.5-1.8°$. Large crystals were observed both in the samples annealed at 700 °C and 1000 °C. The smaller CeO_2 crystals with semi−coherent interfaces are the majority in the samples annealed at 700 °C while the number of large crystals increases at 1000 °C. The distribution density of CeO_2 precipitates increases with the cerium concentration in the melt.

The presence of precipitates induces two negative effects on crystals intended for laser application. On the hand it introduces strains and stresses that reduce optical performance and cannot be removed by low temperature or long annealing [11,22]. Secondly, the precipitates have different refractive coefficient ($n_{CeO2} \approx 2.5$, $n_{NLM} \approx 2.0$) which introduces the light scattering and absorption that impairs the laser action. The precipitation of secondary phases in the crystals used in lasers is still a problem that is difficult to avoid and has not been satisfactorily solved, mainly due to structural defects in real materials [23,24].

There are different reasons for the appearance of light scattering in crystals. For instance, in the case of growth $CaWO_4$ crystals by Czochralski the light scattering may occur owing to the deviation from the stoichiometry to lower WO_3 content in the crystal leading to porosity [25]. It should be noted that $CaWO_4$ is isostructural to NLM which makes it necessary to pay particular attention to such a possibility in our case. Another mechanism one can see in growth from solution KH_2PO_4 (KDP) crystals. It was found that tetragonal KDP crystals may contain the KH_2PO_4 precipitates with orthorhombic structure [26,27]. The phenomenon of the second phase precipitation, similar to that discussed in this paper, was observed in the growth of Lu_2SiO_5 (LSO) and $Lu_{1.8}Y_{0.2}SiO_5$ (LYSO) crystals from the melt by the Czochralski method. Optical and scanning electron microscopy examinations of LSO show the scattering centers to mainly consist of rare-earth oxide inclusions. A lower growth temperature of LYSO produced fewer second phase inclusions [28]. This supports our proposed mechanism. Especially serious problems appear in the growth of laser crystals containing transitional metal ions, one example of which is presented here. In this regard only some technological conditions can be optimized (growth rate, temperature gradients in the system, rate of heating and cooling processes, etc.) to be able only to reduce defect concentration and improve laser damage resistance and increase the transmittance [29].

The electron microscopy observations in this work provide novel information that was not previously available with only X-ray based techniques to verify the presence of Ce oxide precipitates in non-annealed and annealed NLM crystals for laser application. The observation merged SEM, TEM, and STEM approaches, including conventional and atomic resolution, electron diffraction, EDXS, and EELS analysis. These techniques were used to identify and distinguish the second phases (Ce_2O_3 and CeO_2), characterize their size and morphology, and, in fine, their crystallographic relationships and growth directions in the surrounding matrix.

Author Contributions: Conceptualization, E.I.S. and E.V.Z.; methodology, E.I.S. and P.A.B.; validation, K.A.S. and P.A.B.; investigation, E.I.S. and D.A.L.; resources, E.I.S., P.A.B. and K.A.S.; writing—original draft preparation, E.I.S., E.V.Z. and P.A.B.; writing—review and editing, E.I.S. and P.A.B.; supervision, E.V.Z. and P.A.B. All authors have read and agreed to the published version of the manuscript.

Data Availability Statement: Data are available at reasonable request from the authors.

Conflicts of Interest: The authors declare no conflict of interest.

References

1. Rudolph, P. Fundamentals and engineering of defects. *Prog. Cryst. Growth Charact. Mater.* **2016**, *62*, 89–110. [CrossRef]
2. Tuller, H.L.; Bishop, S.R. Point Defects in Oxides: Tailoring Materials Through Defect Engineering. *Annu. Rev. Mater. Res.* **2011**, *41*, 369–398. [CrossRef]
3. Zharikov, E.V.; Zaldo, C.; Díaz, F. Double Tungstate and Molybdate Crystals for Laser and Nonlinear Optical Applications. *MRS Bull.* **2009**, *34*, 271–276. [CrossRef]
4. Kaczmarek, A.M.; van Deun, R. Rare earth tungstate and molybdate compounds—From 0D to 3D architectures. *Chem. Soc. Rev.* **2013**, *42*, 8835–8848. [CrossRef] [PubMed]
5. Loiko, P.A.; Han, X.; Yumashev, K.V.; Kuleshov, N.V.; Serrano, M.D.; Cascales, C.; Zaldo, C. Thermo-optical properties of uniaxial $NaT(XO_4)_2$ laser host crystals (where T = Y, La, Gd or Bi, and X = W or Mo). *Appl. Phys. B* **2013**, *111*, 279–287. [CrossRef]
6. Benoît, G.; Véronique, J.; Arnaud, A.; Alain, G. Luminescence properties of tungstates and molybdates phosphors: Illustration on $ALn(MoO_4)_2$ compounds (A $\frac{1}{4}$ alikaline cation, Ln = lanthanides, M = W, Mo). *Solid State Sci.* **2011**, *13*, 460–467. [CrossRef]
7. Zverev, G.M.; Kolodnyi, G.Y. Stimulated emission and spectroscopic investigations of double lanthanum- sodium molybdate single crystals with neodymium impurities. *J. Exptl. Theoret. Phys. (U.S.S.R.)* **1967**, *52*, 337–341.
8. Stevens, S.B.; Morrison, C.A. $NaLa(MoO_4)_2$ as a laser host material. *Phys. Rev. B* **1991**, *43*, 7386–7394. [CrossRef]
9. Choi, Y.G.; Kim, K.H.; Park, S.H.; Heo, J. Comparative study of energy transfers from Er^{3+} to Ce^{3+} in tellurite and sulfide glasses under 980 nm excitation. *J. Appl. Phys.* **2000**, *88*, 3832–3839. [CrossRef]
10. Sani, E.; Toncelli, A.; Tonelli, M.; Lis, D.A.; Zharikov, E.V.; Subbotin, K.A.; Smirnov, V.A. Effect of cerium co-doping in Er^{3+}, Ce^{3+}: $NaLa(MoO_4)_2$ crystals. *J. Appl. Phys.* **2005**, *97*, 123531. [CrossRef]
11. Kuz'micheva, G.M.; Zharikov, E.V.; Subbotin, K.A.; Lis, D.A.; Rybakov, V.B. X-ray Diffraction Study of the Structure and Defect System of Nominally Pure and Er^{3+}- and Ce^{3+}-Activated $(Na_{0.5}La_{0.5})MoO_4$ Crystals. *Inorg. Mater.* **2005**, *41*, 998–1009. [CrossRef]
12. Suvorova, E.I.; Kuz'micheva, G.M.; Morozkin, A.V.; Zharikov, E.V.; Lis, D.A.; Subbotin, K.A. Microstructure of $(Na_{0.5}La_{0.5})MoO_4$ Crystals Coactivated with Cerium and Erbium Ions. *Inorg. Mater.* **2007**, *43*, 287–291. [CrossRef]
13. Newbury, D.E.; Ritchie, N.W.M. Electron-Excited X-ray Microanalysis by Energy Dispersive Spectrometry at 50: Analytical Accuracy, Precision, Trace Sensitivity, and Quantitative Compositional Mapping. *Microsc. Microanal.* **2019**, *25*, 1075–1105. [CrossRef] [PubMed]
14. Hoeft, H.; Schwaab, P. Investigations towards optimizing EDS analysis by the Cliff-Lorimer method in scanning transmission electron microscopy. *X-ray Spectrom.* **1988**, *17*, 201–208. [CrossRef]
15. Stadelmann, P. JEMS. 2022. Available online: https://www.jems-swiss.ch/ (accessed on 19 January 2023).
16. Boudias, C.; Monceau, D. CaRIne Crystallography 3.1, Description and Trial Version. Available online: http://carine.crystallography.pagesperso-orange.fr/index.html (accessed on 20 June 2023).
17. Artini, C.; Costa, G.A.; Pani, M.; Lausi, A.; Plaisier, J. Structural characterization of the CeO_2/Gd_2O_3 mixed system by synchrotron X-ray diffraction. *J. Solid State Chem.* **2012**, *190*, 24–28. [CrossRef]
18. Bärnighausen, H.; Schiller, G. The crystal structure of A-Ce_2O_3. *J. Less-Common Met.* **1985**, *110*, 385–390. [CrossRef]
19. Garvie, L.A.J.; Xu, H.; Wang, Y.; Putnam, R.L. Synthesis of $(Ca,Ce^{3+},Ce^{4+})2Ti_2O_7$: A Pyrochlore with Mixed-Valence Cerium. *J. Phys. Chem. Solids* **2005**, *66*, 902–905. [CrossRef]
20. Chen, C.-H.; Notis, M.R.; Williams, D.B. Precipitation and solid solubility in the system NiO-Cr_2O_3. *J. Am. Ceram. Soc.* **1983**, *66*, 566–571. [CrossRef]
21. Easterling, K.E.; Johannesson, T. On the Coherency-loss Problem of Growing Precipitates. On the coherency-loss problem of growing precipitates. *Philos. Mag.* **1971**, *24*, 981–986. [CrossRef]
22. Kuz'micheva, G.M.; Rybakov, V.B.; Zharikov, E.V.; Lis, D.A.; Subbotin, K.A. Unusual Structural Properties of $(Na_{0.5}La_{0.5})MoO_4$:Er,Ce Crystals. *Inorg. Mater.* **2006**, *42*, 303–309. [CrossRef]
23. Bohren, C.F.; Huffman, D.R. *Absorption and Scattering of Light by Small Particles*; John Wiley & Sons: Weinheim, Germany, 2008; 544p.
24. Logunov, S.; Kuchinsky, S. Experimental and theoretical study of bulk light scattering in CaF_2 monocrystals. *J. Appl. Phys.* **2005**, *98*, 053501. [CrossRef]
25. Blistanov, A.A.; Zakutalov, K.V.; Ivanov, M.A.; Kvyat, E.V.; Klassen, A.V.; Kochurikhin, V.V.; Yakimova, I.O. Defects in Calcium Tungstate Crystals. *Crystallogr. Rep.* **2006**, *51*, 661–663. [CrossRef]
26. Suvorova, E.I.; Klechkovskaya, V.V. Transmission electron microscopy study of KDP crystals. *Ferroelectrics* **1993**, *144*, 245–253. [CrossRef]
27. Suvorova, E.I.; Chernov, A.A. Anomalous biaxiality and orthorhombic inclusions in KDP crystals. *Crystallogr. Rep.* **1994**, *39*, 827–833.

28. Cooke, D.W.; McClellan, K.J.; Bennett, B.L.; Roper, J.M.; Whittaker, M.T.; Muenchausen, R.E.; Sze, R.C. Crystal growth and optical characterization of cerium-doped $Lu_{1.8}Y_{0.2}SiO_5$. *J. Appl. Phys.* **2000**, *88*, 7360–7362. [CrossRef]
29. Hu, G.; Zhao, Y.; Li, D.; Xiao, Q. Transmittance increase after laser conditioning reveals absorption properties variation in DKDP crystals. *Opt. Express* **2012**, *20*, 25169–25180. [CrossRef]